Patterned optical anisotropic film for generation of non-diffracting vortex beams ⊘

Wei Duan; Ling-Ling Ma; Peng Chen ⓘ ; Wei Hu ⓘ ; Qiong-Hua Wang ✉ ⓘ ; Yan-Qing Lu

Check for updates

View Online   Export Citation

Articles You May Be Interested In

Generation of self-healing and transverse accelerating optical vortices

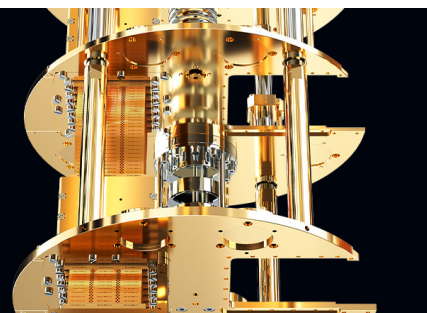*Appl. Phys. Lett.* (September 2016)

Extended Jones matrix method for oblique incidence study of polarization gratings

Appl. Phys. Lett. (July 2012)

Vortex Airy beams directly generated via liquid crystal q-Airy-plates

Appl. Phys. Lett. (March 2018)

Patterned optical anisotropic film for generation of non-diffracting vortex beams

Wei Duan,[1] Ling-Ling Ma,[2] Peng Chen,[2] (iD) Wei Hu,[2] (iD) Qiong-Hua Wang,[1,a] (iD) and Yan-Qing Lu[2,b]

AFFILIATIONS

[1]School of Instrumentation and Optoelectronic Engineering, Beihang University, Beijing 100191, China
[2]College of Engineering and Applied Sciences, Nanjing University, Nanjing 210093, China

[a]Author to whom correspondence should be addressed: qionghua@buaa.edu.cn
[b]E-mail: yqlu@nju.edu.cn

ABSTRACT

Bessel vortex beams (BVBs) are endowed with non-diffracting properties and carry specific orbital angular momentum, which adds a new degree of freedom in the manipulation of light. A patterned liquid crystal polymer (LCP)-based optical anisotropic film is proposed and demonstrated for generation of non-diffracting BVBs. The optical axis distribution is induced by the functionalized film, which can simultaneously modulate the amplitude and phase of the wavefront. Different BVB modes can be obtained in this manner. The topological charges and non-diffracting properties of the BVBs are experimentally verified. The multifunctional LCP film exhibits the merits of low power consumption, low cost, and easy fabrication. It may provide a new strategy for beam shaping and planar optics.

Published under an exclusive license by AIP Publishing. https://doi.org/10.1063/5.0079634

Diffraction occurs when a wave encounters an obstacle or a slit and can be described by the Huygens–Fresnel principle, which concerns the propagating wavefront as a collection of discrete spherical wavelets. In the application fields of laser collimation and processing, precision measurement, and other engineering techniques, it is desirable to use a beam that does not spread in propagation, namely, a non-diffracting beam. Among the various structured optical beams,[1,2] the optical vortex, featuring the phase singularity and helical phase front, has been extensively studied over the past few decades.[3] Its screw-type phase distribution leads to an orbital angular momentum (OAM) of $m\hbar$ per photon,[4] where m represents the topological charge. Such specific beams play a vital role in particle manipulation, optical communication, quantum information, and computation.[5,6] However, optical vortices also suffer from diffraction problems in the propagation process and need a non-diffracting method. A higher-order Bessel beam,[7] known as a Bessel vortex beam (BVB), has been proposed to overcome this obstacle. BVBs have a helical phase factor and are endowed with the non-diffracting property of Bessel beams.[8,9]

To date, there have been several methods developed for generating BVBs.[10–12] A straightforward strategy is to encode a phase singularity into an axicon phase pattern implemented by anisotropic media or anisotropic parameter space, such as a spatial light modulator (SLM) or gradient-index metasurface. Computer-generated hologram-based SLM strategies have great flexibility and tunability, but they suffer from unsuppressed higher diffraction orders, optical inefficiency, and limited beam quality. Beam expansion is a requisite for matching the size of the SLM. Consequently, the SLM consists of numerous separately driven pixels, leading to high cost and relatively complex driving circuits. Another strategy, the metasurface strategy, which is achieved by a nanoimprint or femtosecond laser writing process, can effectively provide geometric phase functions with fixed wavelengths. However, there still exist challenges in reducing fabrication cost, increasing optical efficiency, and achieving dynamic tunability. Thus, more convenient and high-efficiency techniques for BVB generation are in high demand.

Here, we design and fabricate a patterned optical anisotropic film for generation of BVBs in a high-efficient but straightforward way. By encoding an axicon phase profile into a photopatterned liquid crystal polymer (LCP) layer, a BVB (i.e., higher-order Bessel beam) can be generated directly by simultaneously modulating the amplitude and phase of the incident Gaussian beam wavefront. Different modes of BVBs can also be generated in this way, and the diffraction efficiency can theoretically achieve 100% for a high-order Bessel beam. The topological charges and non-diffracting properties of BVBs are experimentally verified and compared with the vortex beams (VBs) generated by the q-plates. Due to the extraordinary thermal and photochemical stability of LCP, non-diffracting BVBs are very efficiently achieved across the visible range. Arbitrary manipulation of the

geometric phase can also be conveniently obtained due to the fidelity and flexibility of the photoalignment technique. This work paves the way for compact configuration and multifunctional non-diffracting optical vortex generation, thus providing an easy but efficient approach for broadband and arbitrary beam shaping in a transmissive manner.[13,14]

A circular polarization grating is introduced into a spiral plate optical axis distribution. This grating modulates the incident polarization states locally and leads to a space-variant geometric phase front, which is also known as the Pancharatnam–Berry (PB) phase.[15,16] We propose a PB-phase LCP functional film, whose optical axis is an integration of an axicon and a q-plate.[17] The optical axes are homogeneous along the z-axis and obey the following equation in the x-y plane:

$$\alpha = -\frac{1}{2}krr + \frac{1}{2}m\varphi, \tag{1}$$

where $r = (x^2 + y^2)^{1/2}$ is the corresponding radius, $\varphi = \arctan(y/x)$ is the azimuthal angle, m is the topological charge, and k_r is the transverse wave vector component. We set $k_r = 10$ (mm)$^{-1}$ in the demonstration.

Referring to the zero-order Bessel beam generated by the axicon,[18] a circular polarization grating is proposed to analogize the modulation of incident light. Figure 1(a) shows the calculated director distributions of the axicon with $\alpha(r) = -k_r r/2$, $k_r = 10$ (mm)$^{-1}$. The gradient color variation from blue to red indicates that the optical axis orientation varies continuously from 0 to π. Figures 1(b) and 1(c) show the q-plate distribution with topological charge values $m = 1$ and $m = 2$. Figures 1(d) and 1(e) show the corresponding optical axis distributions of the integrated spiral axicons for the first- and second-order BVBs, respectively.

The transformation in a spiral axicon can be analyzed using a Jones matrix calculation. The transfer matrix is

$$
\begin{aligned}
\mathbf{T} &= \mathbf{R}(-\alpha) \cdot \begin{bmatrix} \exp(-i\Gamma/2) & 0 \\ 0 & \exp(i\Gamma/2) \end{bmatrix} \cdot \mathbf{R}(\alpha) \\
&= \cos\frac{\Gamma}{2}\mathbf{I} - i\sin\frac{\Gamma}{2}\begin{bmatrix} \cos 2\alpha & \sin 2\alpha \\ \sin 2\alpha & -\cos 2\alpha \end{bmatrix},
\end{aligned} \tag{2}
$$
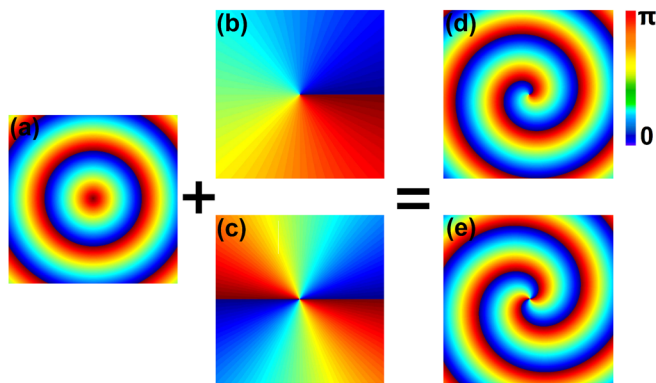
FIG. 1. Optical axis distributions of (a) an axicon, q-plates with (b) $m = 1$, (c) $m = 2$, and integrated spiral axicons with (d) $m = 1$, (e) $m = 2$.

where $\Gamma = 2\pi\Delta nd/\lambda$ is the LCP's phase retardation, Δn is the birefringence, d is the thickness of the LCP layer, and λ is the incident wavelength in free space. Considering a circular incident polarization, which can be described as $\mathbf{E}_{in} = \chi^{(\pm)} = 1/\sqrt{2}(1\pm i)^T$, the two spin eigenstates correspond to the left- and right-hand circular polarization states. After passing through the spiral axicon layer, the output can be expressed as

$$\mathbf{E}_{out} = \mathbf{T} \cdot \mathbf{E}_{in} = \cos\frac{\Gamma}{2} \cdot \chi^{(\pm)} - i\sin\frac{\Gamma}{2} \cdot \exp[\pm im\varphi \mp ikrr] \cdot \chi^{(\mp)}. \tag{3}$$

For a circularly polarized incident beam, Eq. (3) indicates that the output is a superposition of the two parts. The first item maintains the same incident circularly polarized component, while the second component is orthogonal to the incident polarization, and attaches a spiral phase and an axicon phase factor. Under half-wave conditions ($\Gamma = \pi, 3\pi, 5\pi\ldots$), the residual component is completely suppressed, and the output wave is a pure helical high-order Bessel beam, that is, a BVB. Therefore, the circular polarization is, theoretically, 100% transformed to a BVB. Output gain $\pm k_r r$ phase factors for the opposite circularly polarized incident beams. The left-handed/right-handed circular component of the incident beam obtains an additional phase with a radial dependence given by $-k_r r/k_r r$; thus, it exhibits converging and diverging behaviors, respectively. In addition, opposite spiral phases are added to the two orthogonal components, corresponding to BVBs with opposite signs of topological charge m, which is determined by the incident polarization.

A multi-step overlapping exposure method[19,20] is proposed to prepare the designed PB functional film. The fabrication procedure for the LCP film is illustrated in Fig. 2. A digital micro-mirror device-based dynamic lithography system[21] is utilized to implement the photo-alignment process on a polarization-sensitive photoalignment agent. This agent is programmed by using a 0.5 wt. % solution of sulfonic azo-dye SD1 (Dai-Nippon Ink and Chemicals, Japan) dissolved in dimethylformamide and spin-coated on the ultrasonically bathed indium-tin-oxide glass substrate, which is UV-ozone cleaned and cured at 100 °C for 10 min in advance. The SD1 orientation is delivered to adjacent liquid crystal (LC) molecules, which consequently guides the local LC orientation. In addition, SD1 is photo-rewritable, and only the last written polarization information is recorded on the azo-dye layers. SD1 supplies relatively high anchoring energy to the LCs.

After the photo-aligning process, the LCP precursor (UCL017, Dai-Nippon Ink and Chemicals, Japan, 23 wt. % dissolved in methylbenzene) is spin-coated onto the alignment layer. The thickness of the LCP layer is optimized to satisfy the half-wave condition at the target wavelength. Heating over 80 °C is required for residual solvent evaporation. The polymerization of LCP is performed under a 365 nm LED (15 mW/cm², for 2 min). An optical clear adhesive film (8173D, 3M, USA) is attached to the LCP layer to adhere to the functional layer and be separated from the glass substrate. Thus, a self-standing flexible functional LCP film is realized. The obtained LCP film can be used as the oriented layer for the subsequent multi-layer LCP lamination process.

Because it is easy to manipulate the optical axis for PB phase elements, a continuous geometric phase change can be conveniently achieved. Thus, arbitrary wavefront shaping can be realized
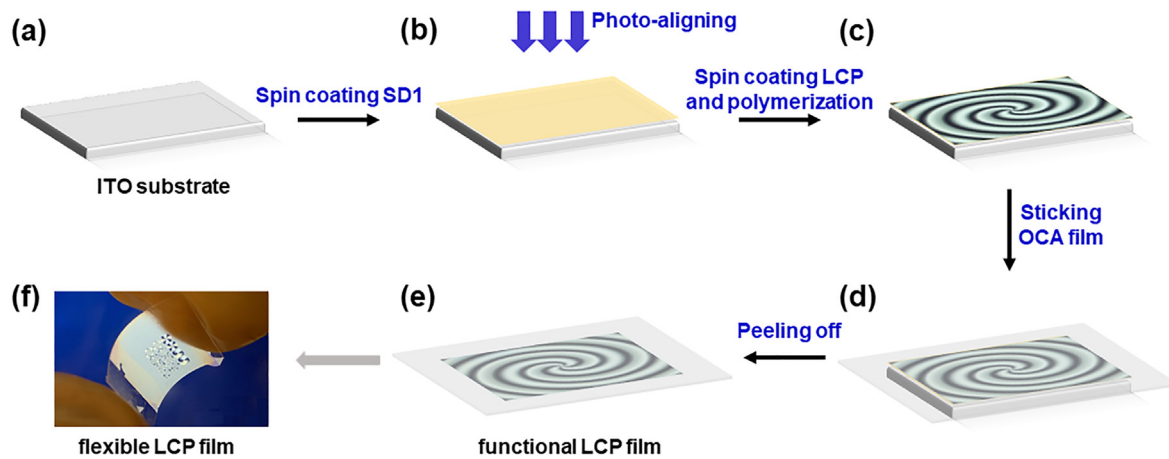
**FIG. 2.** Fabrication process of the BVB spiral axicon plate.

by encoding the desired phase profile into the in-plane optical axis orientations in a flexible and efficient manner. This approach can avoid the shortcomings of conventional contact LC alignment techniques that produce mechanical damage, electrostatic charge, and dust contamination.

The micrographs of the obtained LCP samples under a polarized optical microscope are shown in Figs. 3(c) and 3(d) and 3(g) and 3(h), compared with the theoretical simulation optical axis distributions of different-valued q-plates [Figs. 3(a) and 3(b)] and Bessel vortex templates [Figs. 3(e) and 3(f)]. The continuous variation in micrograph brightness provides a vivid exhibition of the space-variant directors. The dark domains correspond to regions with LC directors approximately perpendicular to the polarizer or analyzer, whereas the bright domains correspond to LC directors at approximately 45° with respect to the polarizer or analyzer. The bright-to-dark alternates twice when

the director changes from 0 to π, leading to denser fringes under the microscope.

When the samples are rotated, the bright and dark domains interconvert gradually, which further manifests the continuous space-variant configuration of the directors. From the microscopic patterns, we can see that spiral structures are obviously introduced, distorting the central orientation of the circular gratings.

All the above samples are placed in the optical setup system for beam generation and analysis. A 473 nm laser beam passes through a polarizer, a quarter-wave plate (QWP), and illuminates the sample. Then, the transmitted light is captured using a charge-coupled device (CCD). The angle between the c-axis of the QWP and the polarization direction is set to $+45°/-45°$ to obtain right-hand/left-hand circular polarization. The BVBs and VBs are generated, and the intensity profiles of the generated BVBs are also detected.
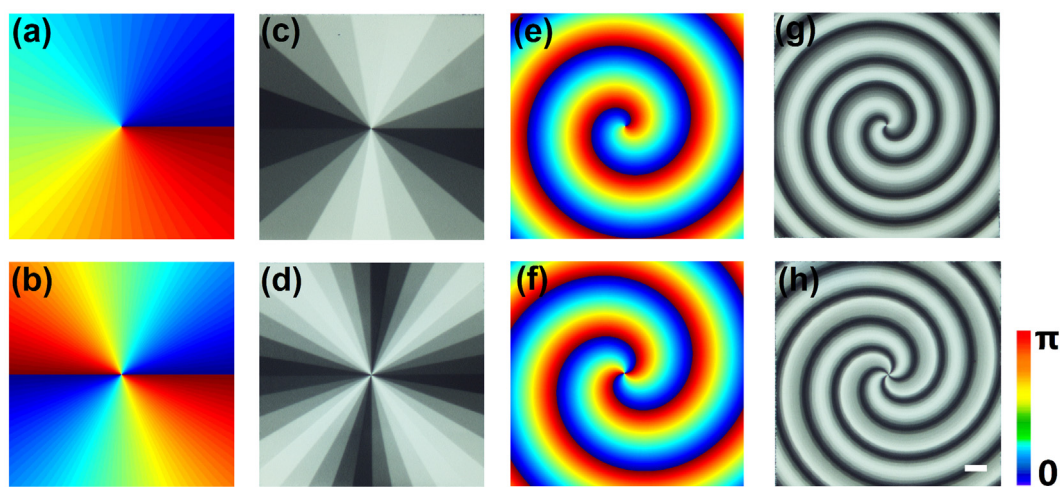
FIG. 3. Calculated optical axis distributions of q-plates: (a) and (b) $m = 1$, $m = 2$, and (c) and (d) corresponding micrographs, (e) and (f) $m = 1$, $m = 2$ valued Bessel vortex templates and (g) and (h) corresponding micrographs under polarized optical microscope. Scale bar: 100 μm.

As expected, Fig. 4(a) shows the beam profiles of the left circular incident polarization BVB and VB, generated at 473 nm. The donut-like intensity profile is due to the phase singularity at the center of the beam, indicating that the half-wave condition is perfectly satisfied ($\Gamma = \pi$). The generated BVB's energy is relatively concentrated compared with the VB's. It can be deduced from Eq. (3) that the transformed component is added by a circular tilted phase factor, $-k_r r$, creating a focused-like beam intensity. Figure 4(b) shows the captured transverse pattern of BVBs that is generated by the left-hand circular polarization incident on the designed LCP functional film with appropriate thickness at three typical wavelengths (473, 532, and 633 nm).

The tunable LCs can be oriented by photosensitive materials, which are sensitive to the change in ultraviolet or blue ultraviolet irradiation of external polarizations and might cause reorienting or rewriting. To address the above issues, a 473 nm half-wave conditional LCP film with different topological charges is fabricated to maintain the orientation after polymerization, thus achieving highly efficient non-diffracting BVBs across the visible range, especially in the photosensitive wavelengths. Subsequently, the left-hand and right-hand circular polarization incidents on the Bessel vortex template are encoded with $m = 2$ and $m = 4$, respectively. The white arrows indicate the incident polarization states, and the emergent beam transverse intensity patterns are captured in the top row of Figs. 4(c) and 4(d). To verify the topological charges of the generated BVBs, a cylindrical lens ($f = 10.0$ cm) is placed in front of the CCD to implement the astigmatic transformation.[22] The converted patterns are captured at the focal plane and presented in the bottom row of Figs. 4(c) and 4(d), where the numbers of dark stripes (marked by white lines) indicate the reversed topological charges resulting from the orthogonal polarization incidents.

Due to the flexibility and stability of the LCP film, it can be spin-coated multiple times to match the designed thickness.[23,24] In addition to all the visible spectra manifested above, these functional films can

be adopted in a wide range of wavebands, not only in the ultraviolet spectrum but also in the infrared and terahertz bands.

To verify the non-diffracting property, the BVB propagation dynamics with $m = 1$ in free space are analyzed and compared with the VB generated by the q-plate. In this experiment, we fix the position of the LCP samples and defined the same initial coordinate (denoted as $d = 0$ cm) of the output plane along the normal incident direction. In the calculated theoretical maximum non-diffracting region, the CCD is parallel shifted an interval distance to capture the two generated sets of beams in a valid detected area. The two captured series of beam profiles in different positions, and the intensity variations along the propagation, are depicted in Fig. 5. By comparing Figs. 5(a) and 5(b), it can be seen that for an identical incident, the generated BVB has a narrower full width at half maximum (FWHM) than the VB. The energy distribution of the BVB is relatively concentrated compared with that of the VB, due to the added axicon phase factor.

In addition, the variations in the normalized intensity integrations and FWHMs of the two beams are depicted and presented in Fig. 6. The fitted curves with circular/triangle symbols indicate the BVB/VB diffractive information. Normalized intensity and FWHM variations are recorded using the black and blue sets of statistics. The results show that the two beams possess the same intensity at the initial position. However, the BVB's curve has a smaller slope than the VB's, indicating that the BVB has less intensity attenuation than the VB. The FWHM of the BVB also increased more slowly than that of the VB. All the above statistics indicate that the generated BVB notably improves the non-diffracting characteristics. For an ideal BVB, which is infinite in energy and space, the beam profile is theoretically invariable in propagation. Only quasi-nondiffracting phenomena and properties are observed experimentally.

A strategy for non-diffracting BVBs generation via an integrated LCP film is demonstrated. It saves the space of the optical path system
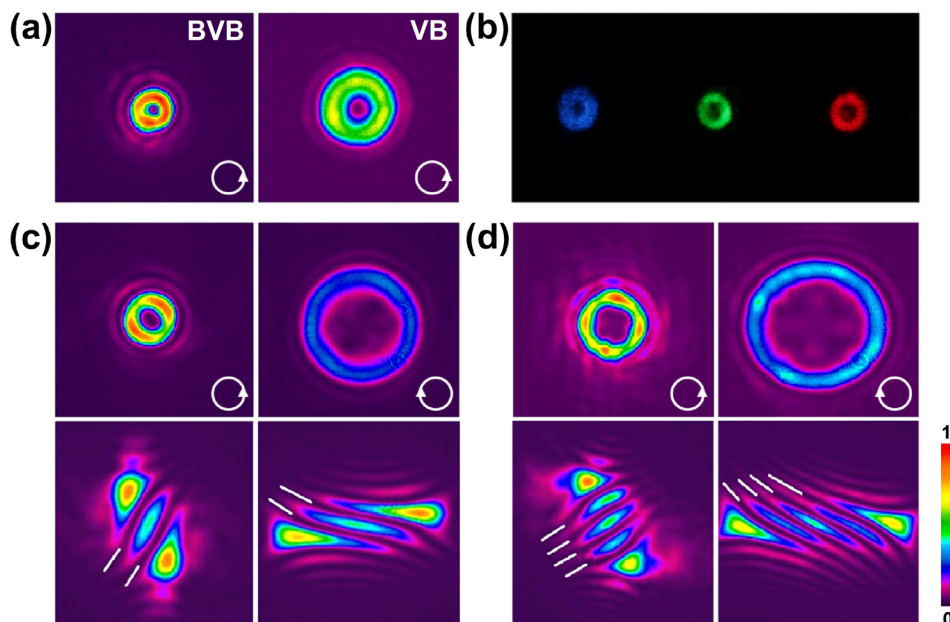
FIG. 4. (a) Diffracted beam profiles of a generated BVB (left side) and VB (right side), (b) the diffraction patterns of generated BVBs at three typical laser wavelengths (473, 532, and 633 nm), the captured diffraction intensity (top row) and astigmatic transformation (bottom row) patterns of BVBs with (c) $m = \pm 2$ and (d) $m = \pm 4$.
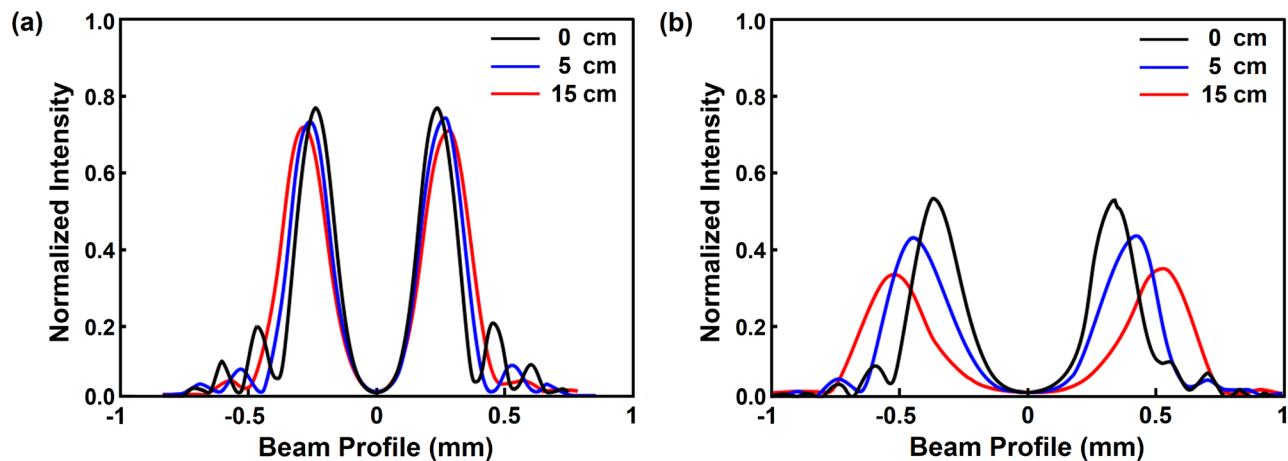
FIG. 5. Intensity profiles of (a) BVB and (b) VB in the propagation distance 0, 5, and 15 cm, respectively.
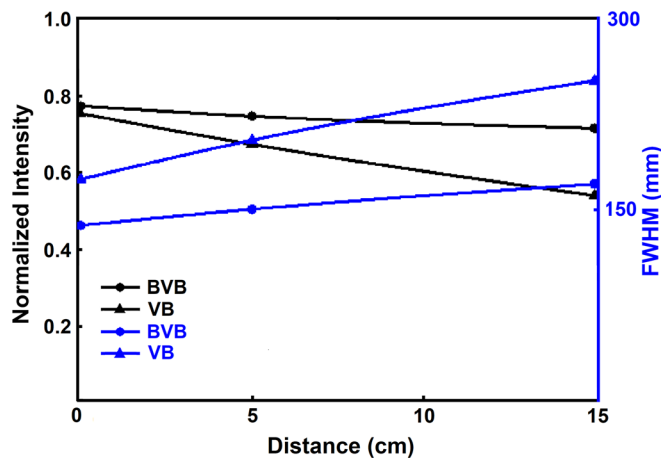

FIG. 6. Normalized intensity and FWHM variations along the propagation distances.

and overcomes the mismatch caused by mechanical processes. Due to the good stability and flexibility of the LCP film, the LCP can be spin-coated multiple times to match the designed thickness. In addition to the visible band we reported, these functional films can be adopted in a wide range of wavebands, not only in the ultraviolet spectrum, but also in the infrared and terahertz bands.

In summary, a patterned LCP-based optical anisotropic film is proposed and demonstrated for non-diffracting BVB generation. The quasi-nondiffracting properties of BVBs have been verified both theoretically and experimentally. The multifunctional LCP film also has the advantages of low power consumption, low cost, and easy fabrication and provides a possible strategy for geometric phase optical elements or arbitrary wavefront shaping for optical communication, particle manipulation, microscopic imaging, and other fields.

AUTHOR DECLARATIONS

Conflict of Interest

The authors have no conflicts to disclose.

DATA AVAILABILITY

The data that support the findings of this study are available from the corresponding author upon reasonable request.

REFERENCES

[1]H. R. Dunlop, A. Forbes, M. V. Berry, M. R. Dennis, D. L. Andrews, M. Mansuripur, C. Denz, C. Alpmann, P. Banzer, T. Bauer, E. Karimi, L. Marrucci, M. Padgett, M. R. Marte, N. M. Litchinitser, N. P. Bigelow, C. R. Guzmán, A. Belmonte, J. P. Torres, T. W. Neely, M. Baker, R. Gordon, A. B. Stilgoe, J. Romero, A. G. White, R. Fickler, A. E. Willner, G. Xie, B. McMorran, and A. M. Weiner, J. Opt. **19**(1), 013001 (2017).
[2]A. Forbes, M. D. Oliveira, and M. R. Dennis, Nat. Photonics **15**, 253–262 (2021).
[3]Y. J. Shen, X. J. Wang, Z. W. Xie, C. J. Min, X. Fu, Q. Liu, M. L. Gong, and X. C. Yuan, Light Sci. Appl. **8**, 90 (2019).
[4]L. Allen, M. W. Beijersbergen, R. J. C. Spreeuw, and J. P. Woerdman, Phys. Rev. A **45**(11), 8185 (1992).
[5]A. M. Yao and M. J. Padgett, Adv. Opt. Photonics **3**(2), 161–204 (2011).
[6]X. L. Wang, X. D. Cai, Z. E. Su, M. C. Chen, D. Wu, L. Li, N. L. Liu, C. Y. Lu, and J. W. Pan, Nature **518**, 516–519 (2015).
[7]D. McGloin and K. Dholakia, Contemp. Phys. **46**(1), 15–28 (2005).
[8]J. Durnin, J. Opt. Soc. Am. A **4**, 651 (1987).
[9]J. Durnin, J. Miceli, and J. H. Eberly, Phys. Rev. Lett. **58**(15), 1499–1501 (1987).
[10]J. A. Davis, J. Guertin, and D. M. Cottrell, Appl. Opt. **32**(31), 6368–6370 (1993).
[11]J. Arlt and K. Dholakia, Opt. Commun. **177**(1), 297–301 (2000).
[12]Y. Shen, J. Yang, H. Meng, W. Dou, and S. Hu, Appl. Phys. Lett. **112**(14), 141901 (2018).
[13]H. Q. Zhang, W. Duan, C. T. Xu, and W. Hu, Crystals **10**, 882 (2020).
[14]A. J. Hess, G. Poy, J. B. Tai, S. Žumer, and I. I. Smalyukh, Phys. Rev. X **10**, 031042 (2020).
[15]S. Pancharatnam, Proc. Indian Acad. Sci., Sect. A **44**, 247–262 (1956).
[16]M. V. Berry, J. Mod. Opt. **34**(11), 1401–1407 (1987).

14 May 2025 10:44:08

[17]W. Ji, C. H. Lee, P. Chen, W. Hu, Y. Ming, L. Zhang, T. H. Lin, V. Chigrinov, and Y. Q. Lu, Sci. Rep. **6**(1), 25528 (2016).

[18]G. Scott and N. McArdle, Opt. Eng. **31**(12), 2640–2644 (1992).

[19]W. Duan, P. Chen, S. J. Ge, B. Y. Wei, W. Hu, and Y. Q. Lu, Opt. Express **25**(13), 14059–14064 (2017).

[20]P. Chen, L. L. Ma, W. Hu, Z. X. Shen, H. K. Bisoyi, S. B. Wu, S. J. Ge, Q. Li, and Y. Q. Lu, Nat. Commun. **10**, 2518 (2019).

[21]H. Wu, W. Hu, H. C. Hu, X. W. Lin, G. Zhu, J. W. Choi, V. Chigrinov, and Y. Q. Lu, Opt. Express **20**(15), 16684–16689 (2012).

[22]V. Denisenko, V. Shvedov, A. Desyatnikov, D. Neshev, W. Krolikowski, A. Volyar, M. Soskin, and Y. Kivshar, Opt. Express **17**(26), 23374–23379 (2009).

[23]T. Zhan, J. Y. Zou, J. H. Xiong, X. M. Liu, H. Chen, J. L. Yang, S. Liu, Y. J. Dong, and S. T. Wu, Adv. Opt. Mater. **8**, 1901360 (2020).

[24]J. Y. Zou, T. Zhan, J. H. Xiong, and S. T. Wu, Opt. Express **28**, 4921 (2020).

14 May 2025 10:44:08